Journal of the Korean Ceramic Society
Vol. 55, No. 5, pp. 461–472, 2018.

https://doi.org/10.4191/kcers.2018.55.5.09

Aerosol Synthesis of Gd_2O_3:Eu/Bi Nanophosphor for Preparation of Photofunctional Pearl Pigment as Security Material

Kyeong Youl Jung*,†, Jang Hoon Han*, Dae Sung Kim, Byung-Ki Choi***, and Wkang-Jung Kang*****

*Department of Chemical Engineering, Kongju National University, Cheonan 31080, Korea
**Eco-composite Materials Center, Korea Institute of Ceramic Engineering and Technology (KICET), Jinju 52851, Korea
***CQV Co., Ltd, Jinchen 27845, Korea

(Received June 7, 2018; Revised August 23, 2018; Accepted August 23, 2018)

ABSTRACT

Gd_2O_3:Eu/Bi nanoparticles were synthesized via spray pyrolysis and applied for the preparation of a luminescent pearl pigment as an anti-counterfeiting material. The luminescence properties were optimized by changing the Eu^{3+} and Bi^{3+} concentration. Ethylene glycol was used as an organic additive to prepare the Gd_2O_3:Eu/Bi nanoparticles. The highest emission intensity was achieved when the total dopant content was 10.0 at.% and the mole fraction of Bi was 0.1. The concentration quenching was mainly due to dipole–dipole interactions between the same activators, and the critical distances were 9.0 and 19.6 Å for Eu^{3+} and Bi^{3+}, respectively. The prepared Gd_2O_3:Eu/Bi powder exhibited an average size of approximately 82.5 nm and a narrow size distribution. Finally, the Gd_2O_3:Eu/Bi nanophosphor coated on the surface of the pearl pigment was confirmed to have good red emission under irradiation from a portable ultraviolet light-emitting diode lamp (365 nm).

Key words : Spray pyrolysis, Nanophosphor, Pearl pigment, Anti-counterfeiting

1. Introduction

As the global economy grows, the counterfeiting of products and important documents raises economic and social issues and is considered as a critical problem that violates the intellectual property rights of companies and confuses the order of the market economy. To overcome this problem, many efforts are dedicated to the development of anti-counterfeiting technologies, including unique markers, holograms, plasmonic labels, and security inks.[1–4] When introducing a security substance, it is necessary to maintain the function or quality of the products. In addition, to achieve full functionality as an advanced anti-counterfeiting technology, security materials should have various and complex characteristics. One of the most effective ways to prevent counterfeiting is to print a unique security code using materials that are difficult to imitate.[5,6] Thus, fluorescent materials are effective anti-counterfeiting materials.[7–11] Lanthanide-based phosphor nanoparticles have attracted considerable attention as potential security materials because they have excellent emission characteristics under ultraviolet (UV) or infrared excitation, good thermal and chemical stability, and easy synthesis.

Pearlescent pigments have various applications, such as specialty paper, printing inks, cosmetics, and automotive paints.[12,13] Typically, pearl pigments consist of a two-dimensional substrate (e.g., Mica) with a low refractive index and coating layers (e.g., TiO_2) with a high refractive index.[14–17] The pearl effect or color can be controlled by changing the thickness of the high-refractive index coating layer. The pearlescent pigment can be used as a security material owing to its unique sparkling effect or color change depending on the angle of illumination. If the pearlescent pigment is functionalized by a luminescent substance, it can have its own security function without the help of additional anti-counterfeiting marks. Luminescent pearl pigments are expected to be used as next-generation anti-counterfeiting materials.[18] There are two ways to make luminescent pearl pigments. One is to make the pearlescent pigment have its own fluorescent property by doping the luminescent activator, and the other is to coat the surface of the pearl pigment with phosphor nanoparticles having high luminescence. The latter method is easier than the former method. To prevent the degradation of the optical properties of the pearlescent pigment due to the phosphor coating, the phosphor particles should have both a fine size and a high luminescent property.

Eu-doped Gd_2O_3 (Gd_2O_3:Eu) is known to have good red emission owing to the $^5D_0 \rightarrow {}^7F_j$ transition of Eu^{3+} under 254-nm UV excitation.[19] If the nanosize Gd_2O_3:Eu particles themselves are used as a security marking material, the light-emission characteristics can easily be confirmed using a 254-nm portable hand UV lamp. However, as the particle size is reduced to the nanometer level, the emission inten-

†Corresponding author : Kyeong Youl Jung
E-mail : kyjung@kongju.ac.kr
Tel : +82-41-521-9365 Fax : +82-41-554-2640

sity of the phosphor is greatly reduced.[20] In addition, when a small amount of nanophosphor is coated on a product such as a pearl pigment, a high-power UV lamp is needed to obtain high emission visible to the naked eye. Currently, portable light-emitting diode (LED) lamps with a high output power of 365 nm are commercially available and can be easily utilized as a light source. Therefore, it is more advantageous for the nanophosphors to have high luminescence characteristics under 365-nm UV irradiation than under 254-nm UV irradiation. To control the excitation characteristics, it is necessary to use a sensitizer in the energy transfer with Eu^{3+}. For Eu-doped oxides, including Y_2O_3, Gd_2O_3, YVO_4, and $CaZrO_3$, the codopant Bi^{3+} is well known to act as a sensitizer for the energy transfer from Bi^{3+} to Eu^{3+} under near-UV excitation.[21–24] Therefore, Eu/Bi-doped oxides show red emission due to the $^5D_0 \rightarrow {}^7F_j$ transition of Eu^{3+} under UV excitation in the range of 300 to 400 nm.

Gd_2O_3:Eu nanoparticles have been synthesized via the sol-gel, precipitation, and combustion methods.[25-27] The luminescence properties of phosphors having two or more dopants are strongly influenced by the distribution of activators and sensitizers in the host matrix. As a result, even if the phosphor composition is the same, the luminescence properties can differ depending on the synthesis method. In general, it is necessary to uniformly distribute the dopant throughout the host matrix in order to obtain excellent luminescent characteristics. Thus, spray pyrolysis is considered as a good synthesis method for multi-component functional materials such as phosphor.[28–30] In spray pyrolysis, one particle is generated from one droplet, and all ingredients within the droplet can be mixed on a molecular level. As a result, spray pyrolysis allows the production of phosphor particles having high crystallinity and a uniform distribution of the dopant without forming an impurity phase. In particular, when spray pyrolysis is applied to the synthesis of phosphors with two or more dopants, each dopant can be uniformly distributed throughout the phosphor particles without localized separation. By introducing an appropriate organic additive into the spraying solution, nanoparticles can be easily produced via spray pyrolysis. For example, the addition of ethylene glycol (EG) to the spraying solution produces hollow particles with thin shells, and after the heat treatment, the thin shells crystallize into less agglomerated nanoparticles.[31–33] The aggregates can be easily turned into individual nanoparticles through a simple milling process. To our knowledge, there is no research on the synthesis of Gd_2O_3:Eu/Bi nanoparticles via spray pyrolysis and their application to the preparation of fluorescent pearl pigments.

In this study, Gd_2O_3:Eu/Bi nanoparticles were prepared via spray pyrolysis, and the luminescence properties were investigated by controlling the concentration of the activator and sensitizer. Similar to Y_2O_3:Eu/Bi, the energy transfer between Bi^{3+} and Eu^{3+} was identified to occur in the Gd_2O_3 host. The dopant concentration was optimized to obtain the highest luminescence under 365-nm UV excitation. EG was introduced into the spray solution to prepare nanosize Gd_2O_3:Eu/Bi powder, and the EG concentration was varied to investigate changes in the particle size and luminescence properties. Gd_2O_3:Eu/Bi nanoparticles with an average particle size of 100 nm or less were coated on the plate-shaped pearl pigment, and their luminescence properties were investigated under a commercially available 365-nm LED hand lamp. Finally, it was confirmed that Gd_2O_3:Eu/Bi nanoparticles prepared via spray pyrolysis can be applied to the preparation of photofunctional pearl pigments having an anti-counterfeiting function.

2. Experimental Procedure

2.1. Materials and synthesis of Gd_2O_3:Eu/Bi nanoparticles

Gd_2O_3:Eu/Bi nanoparticles were prepared via a spray pyrolysis process. Gadolinium (III) oxide (Gd_2O_3, Alfa, 99.99%), Europium (III) oxide (Eu_2O_3, Alfa, 99.99%), bismuth(III) nitrate ($Bi(NO_3)_3$, Alfa, 98%), and EG (Sigma-Aldrich, 98%) were used as starting materials. The pearl pigment—TiO_2-coated mica (CQV Co., Ltd.)—was used as the coating substrate of the nanophosphor. Gd_2O_3 or Eu_2O_3 was first dissolved as a nitrate form by using HNO_3 with a small amount of water. To prepare the spray solution, purified water was added to the Gd_2O_3/Eu_2O_3-dissolved solution, followed by dissolving bismuth nitrate and EG. The total precursor concentration was 0.3 M. The Eu content (x) in $(Gd_{2-x}, Eu_x)O_3$ was varied from 0.1 to 0.3. The Bi content (y) in $(Gd_{2-x-y}, Eu_x, Bi_y)O_3$ was changed from 0.01 to 0.06 at x = 0.2 or 0.175. The EG concentration was varied from 0.075 M to 0.45 M. Therefore, the EG/Gd molar ratio was adjusted from 0.25 to 1.5 for the 0.3 M Gd solution. The spray pyrolysis equipment used consisted of an aerosol generator, a quartz tube (ID = 50 mm and L = 1,200 mm) and a Teflon bag filter. The prepared spray solution was atomized with an ultrasonic nebulizer (1.7 MHz), and the resulting droplets were carried to the quartz reactor maintained at 900°C with air (40 *l*/min). The particles produced by drying and pyrolysis were collected by a Teflon bag filter mounted at the end of a quartz reactor and calcined at 1,000°C for 3 h in an air environment.

The prepared Gd_2O_3:Eu/Bi nanoparticles were coated on the surface of the pearlescent pigment in an aqueous medium. The phosphor powder was dispersed in purified water (200 mL), followed by ultrasonic treatment for 30 min. The pigment powder (3 g) was also dispersed in purified water (300 mL). The pH of each solution was adjusted to 8.0 by adding a diluted ammonia solution. Then, the solution containing phosphor nanoparticles was slowly added to the pigment-dispersed solution with vigorous agitation. The weight percentage of the phosphor nanopowder with respect to the pigment was adjusted from 5.0% to 15.0%. After the mixed solution was agitated for 1 h, the resulting solid powder was withdrawn using a vacuum evaporator and dried in a convection oven at 50°C.

2.2. Characterization

The photoluminescence and optical reflectance spectra were measured using a spectrophotometer (PerkinElmer LS 50) and a UV–visible (UV–vis) spectrophotometer (Shimadzu 2540), respectively. The particle-size distribution was measured using a particle-size analyzer (ELS-Z, Otsuka). The crystal structure, morphology, and microstructure of the prepared Gd_2O_3:Eu/Bi particles were investigated via X-ray diffraction (XRD, Rigaku, MiniFlex 600), scanning electron microscopy (SEM, Hitachi S4800), and field-emission transmission electron microscopy (TEM, JEOL-2100F), respectively. For pearl pigments coated with Gd_2O_3:Eu/Bi nanoparticles, the red emission was confirmed by illumination from a commercially available 365-nm LED lamp.

3. Results and Discussion

3.1. Luminescence properties of Gd_2O_3:Eu

Figure 1 shows the luminescence characteristics of Gd_2O_3:Eu phosphors prepared with different Eu contents. The emission was measured at the excitation wavelength of 254 nm, and the excitation was monitored at the emission wavelength of 613 nm. The sharp emission peaks observed ranging from 550 to 750 nm are due to a typical $^5D_0 \rightarrow {}^7F_j$ (j = 0, 1, 2, 3, 4) transition of Eu^{3+} ions. In the excitation spectrum (Fig. 1(b)), the strong peak from 230 to 265 nm is due to the charge-transfer band (CTB) of $O^{2-}(2p) \rightarrow Eu^{3+}$ (4f). The shoulder peak around 280 nm is attributed to the $^8S_{7/2} \rightarrow {}^6I_J$ transition of Gd^{3+}, and the small peak at 315 nm corresponds to the $^8S_{7/2} \rightarrow {}^6P_J$ transition of Gd^{3+}, which is known as the result of Gd^{3+}-Eu^{3+} energy transfer. The weak peaks from 350 to 550 nm are due to the f-f transition of Eu^{3+}. Fig. 1(c) shows the dependency of the emission (λ_{ex} = 254 nm) on the Eu concentration. The luminescence intensity reaches a maximum at x = 0.2 (10.0 at.%). Referring to previous studies in which Gd_2O_3:Eu was synthesized via sol-gel, precipitation, and combustion methods,[34,35] the optimum Eu^{3+} content is 7–8%. On the other hand, when Gd_2O_3:Eu^{3+} is synthesized via spray pyrolysis, the optimum Eu^{3+} content for achieving the highest luminescence is 10% in this work. This indicates that a highly uniform distribution of Eu^{3+} in Gd_2O_3 is achieved for preparation via spray pyrolysis. In general, when the Eu content increases above a critical concentration, concentration quenching of the luminescence intensity occurs as a result of non-radiative energy transfer from one Eu^{3+} ion to another. The non-radiative energy transfer between Eu^{3+} ions can occur through the exchange interaction or multipole–multipole interaction. The interaction mechanism involved in the concentration quenching can be identified via calculation of the critical distance (R_c)

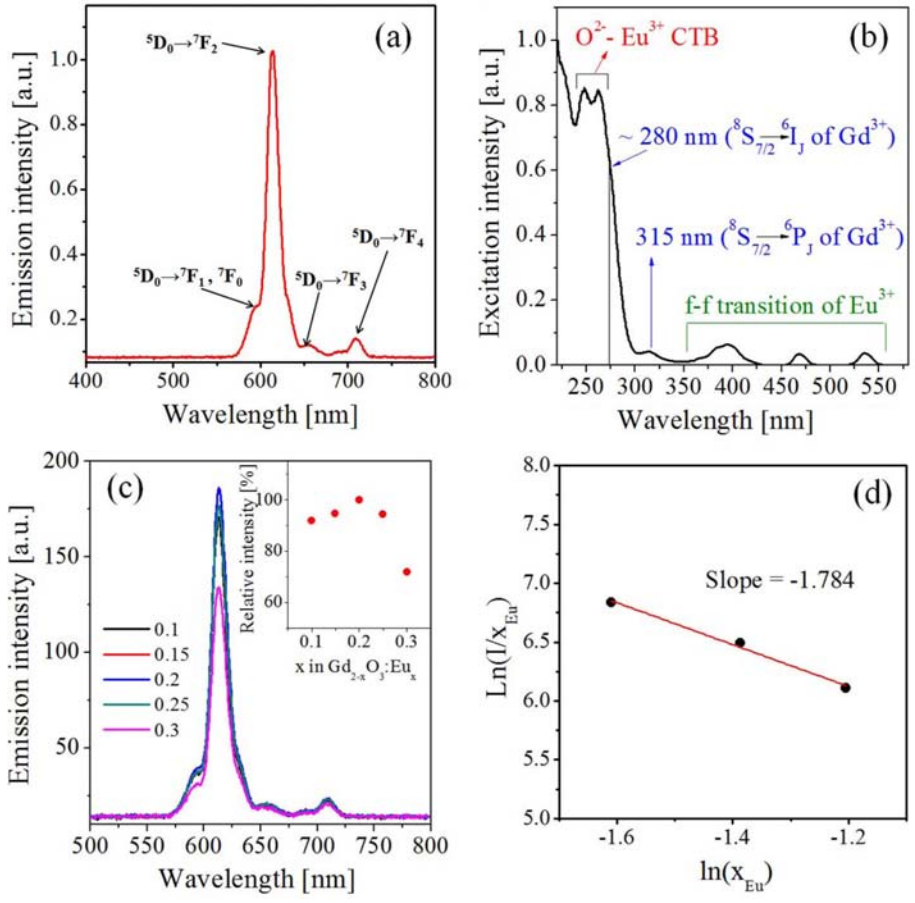

Fig. 1. Luminescence properties of Gd_2O_3:Eu prepared via spray pyrolysis: (a) emission spectrum (λ_{ex} = 254 nm), (b) excitation spectrum (λ_{em} = 613 nm), (c) effect of Eu^{3+} concentration on the emission, and (d) plot of ln(I/x) vs. ln(x).

between Eu^{3+} ions.[33]

$$R_c = 2\left(\frac{3V}{4\pi X_c N}\right)^{1/3} \quad (1)$$

Here, V and N are the unit cell volume and the number of sites available for the Eu^{3+} substitution in the unit cell, respectively. X_c is the critical mole fraction of Eu^{3+} substituted at the Gd^{3+} site of the unit cell. Thus, X_c = x/2 in $(Gd_{2-x}, Eu_x)O_3$. Then, the critical distance (R_c) is calculated as approximately 9.1 Å at x = 0.2. Non-radiative energy transfer via the exchange interaction is generally possible when the critical distance is 5 Å or shorter. Therefore, the concentration quenching in the emission intensity of Gd_2O_3:Eu is caused by the multipole–multipole interaction. The multipole interaction can be elucidated from the following relationship between the emission intensity and the activator concentration (x):

$$\frac{I}{x} = \frac{K}{1+\beta x^{Q/3}} \quad (2)$$

where Q is the interaction character, which is 6, 8, and 10 for the dipole–dipole, dipole–quadrupole, and quadrupole–quadrupole interactions, respectively. K and β are the interaction constants. The Q value can be estimated according to the slope of the plot of $\ln(I/x)$ vs. $\ln(x)$, under the assumption that $\beta x^{Q/3} >> 1$. As shown in Fig. 1(d), the slope is - 1.784, and the resulting Q is approximately 5.349. That is, the calculated Q value is close to 6, indicating that the concentration quenching is mainly caused by the dipole–dipole interaction.

3.2. Luminescence optimization of Gd_2O_3:Eu/Bi

Figure 2 shows the excitation and emission spectra of Gd_2O_3:Bi, Gd_2O_3:Eu, and Gd_2O_3:Eu/Bi. As shown in Fig. 2(a), Gd_2O_3:Bi has a strong excitation peak (λ_{max} = 342 nm) between 300 and 380 nm due to the $^1S_0 \rightarrow {}^1P_1$ transition of Bi^{3+}, and it shows a broad emission between 400 and 700 nm due to the $^3P_1 \rightarrow {}^1S_0$ transition.[22] The emission spectrum of Gd_2O_3:Bi, which was monitored at λ_{ex} = 342 nm, consists of two emission bands with peaks at 420 and 515 nm. This is because Bi^{3+} ions are located at two different sites (C_2 and S_6) of the cubic Gd_2O_3 host.[36] The emission peaks observed at 420 and 515 nm correspond to Bi^{3+} located at the S_6 and C_2 sites, respectively. Fig. 2(b) shows the excitation spectrum of Gd_2O_3:Eu and the emission spectrum of Gd_2O_3:Bi. The three excitation peaks of Gd_2O_3:Eu^{3+} observed between 350 and 580 nm overlap significantly with the emission spectrum of Gd_2O_3:Bi^{3+}, indicating that resonance energy

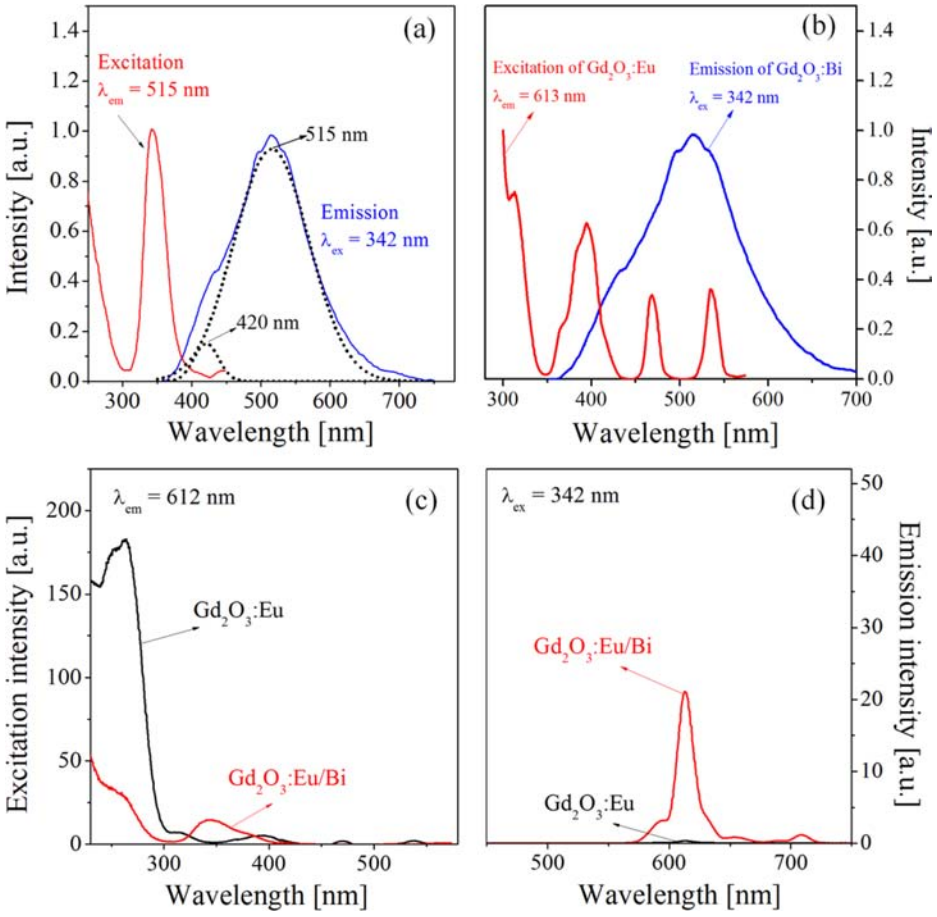

Fig. 2. Photoluminescence spectra: (a) excitation and emission of Gd_2O_3:Bi; (b) excitation of Gd_2O_3:Eu and emission of Gd_2O_3:Bi. (c) excitation and (d) emission of Gd_2O_3:Eu and Gd_2O_3:Eu/Bi particles prepared via spray pyrolysis.

transfer from Bi^{3+} to Eu^{3+} can occur in the Gd_2O_3 host. In Fig. 2(c), which shows the excitation spectrum of Gd_2O_3:Eu/Bi measured at the emission wavelength of 612 nm, the peak near 342 nm corresponding to the $^1S_0 \rightarrow {}^1P_1$ transition of Bi^{3+} becomes strong, while the CTB of $O^{2-}(2p) \rightarrow Eu^{3+}$ (4f) is greatly reduced. Consequently, the red emission peak of Gd_2O_3:Eu/Bi under 342-nm excitation is significantly larger than that of Gd_2O_3:Eu due to the energy transfer from Bi^{3+} to Eu^{3+} (Fig. 2(d)).

Figure 3 shows XRD and UV–vis reflectance spectra of Gd_2O_3:Eu, Gd_2O_3:Bi, and Gd_2O_3:Eu/Bi particles. In the XRD results, the observed peaks are well matched with the cubic Gd_2O_3 phase (JCPDS # 12-0797) without an impurity phase, indicating that the activators are homogenously substituted in the host lattice. The crystallite sizes and lattice constants are calculated from the XRD data peak of the (222) phase, and the resulting values are displayed in Fig. 3(b). The lattice constant (a) was calculated using the following equation:

$$d^2 = \frac{a^2}{h^2+l^2+k^2} \quad d = 0.5\lambda/\sin\theta \tag{3}$$

where d is the interplanar distance, λ is the incident wavelength, θ is the Bragg angle, and h, l, and k are the Miller indices. The resulting lattice constants are 10.781 Å, 10.804 Å, and 10.801 Å for Gd_2O_3:Eu, Gd_2O_3:Bi, and Gd_2O_3:Eu/Bi, respectively. The radii of Eu^{3+} (0.109 nm) and Bi^{3+} (0.117 nm) are similar to that of Gd^{3+} (0.108 nm). Therefore, Gd^{3+}, Eu^{3+}, and Bi^{3+} can form a solid solution in the Gd_2O_3 host lattice, which agrees well with the fact that there is no detectable change in the XRD data with the doping of Eu^{3+} and Bi^{3+}. The crystallite size decreases slightly with the Bi^{3+} doping, but the lattice constant remains almost unchanged. According to the UV–vis reflectance spectra (Fig. 3(c)), Gd_2O_3 has small peaks at 276 and 312 nm due to the $^8S_{7/2} \rightarrow {}^6I_j$ and $^8S_{7/2} \rightarrow {}^6P_j$ transitions of Gd^{3+} ions, respectively. The intense absorption peaks at 255 nm for Gd_2O_3:Eu and 267 nm for Gd_2O_3:Eu/Bi are attributed to the O^{2-}–Eu^{3+} charge transfer. Both Gd_2O_3:Bi and Gd_2O_3:Eu/Bi have an intense absorption peak at 340 nm and a shoulder peak around 385 nm, which are due to the $^1S_0 \rightarrow {}^1P_1$ transition of Bi^{3+} located at the C_2 and S_6 sites of Gd_2O_3, respectively. For the Gd_2O_3:Eu/Bi sample, the absorbance and excitation spectra

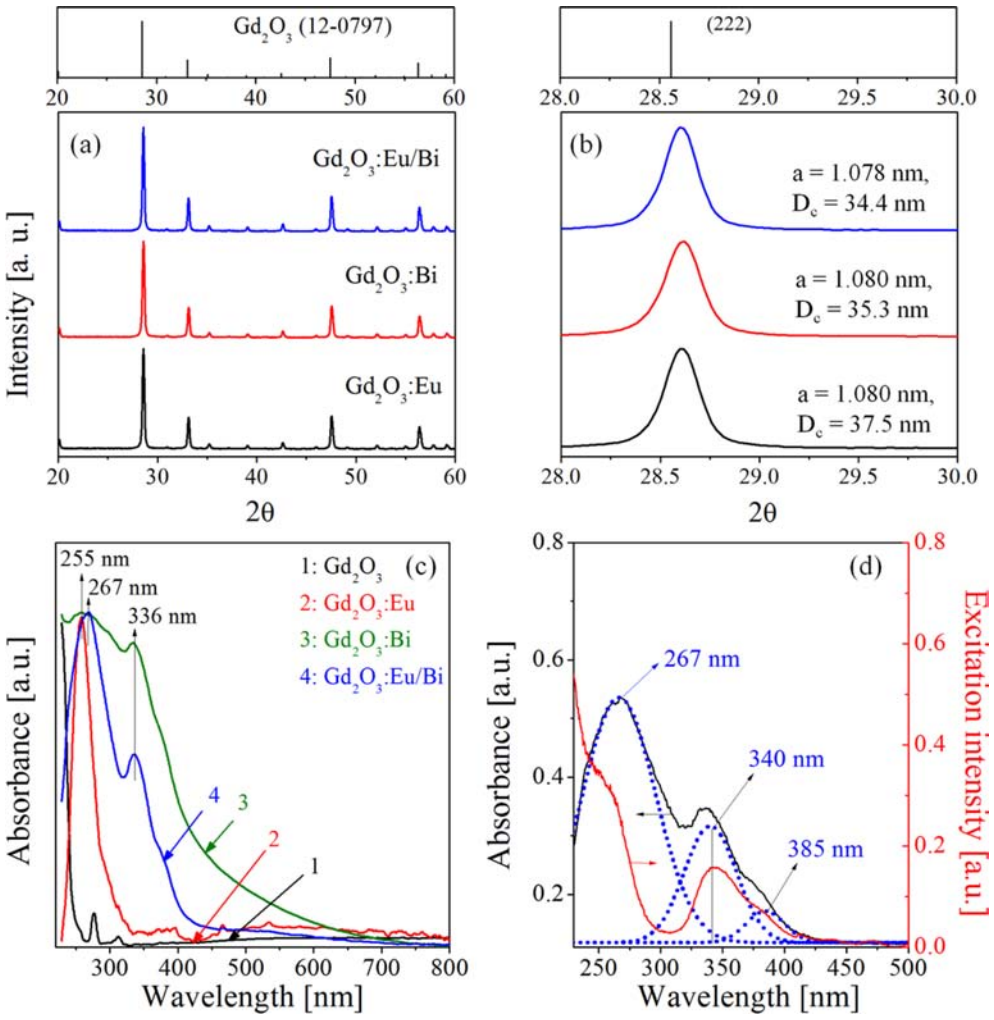

Fig. 3. (a) XRD patterns, (b) peaks for the (222) plane, and (c) UV–vis absorption spectra for Gd_2O_3:Bi, Gd_2O_3:Eu, and Gd_2O_3:Eu/Bi. (d) comparison of the UV–vis absorption with the excitation spectrum for Gd_2O_3:Eu/Bi.

are compared in Fig. 3(d). The absorbance spectrum consists of three main peaks at 267, 340, and 385 nm. These peaks agree well with the excitation peaks.

To maximize the red emission of $Gd_{2-x-y}O_3:Eu_x/Bi_y$ due to the energy transfer from Bi^{3+} to Eu^{3+}, the Bi content (y) was varied at the Eu contents of x = 0.2 and x = 0.175. Additionally, the emission intensity was monitored while changing the ratio of Bi to Eu when the total dopant concentration was fixed at x + y = 0.2. Figs. 4(a)–(c) show the emission spectra obtained under the 340-nm excitation. Fig. 4(d)

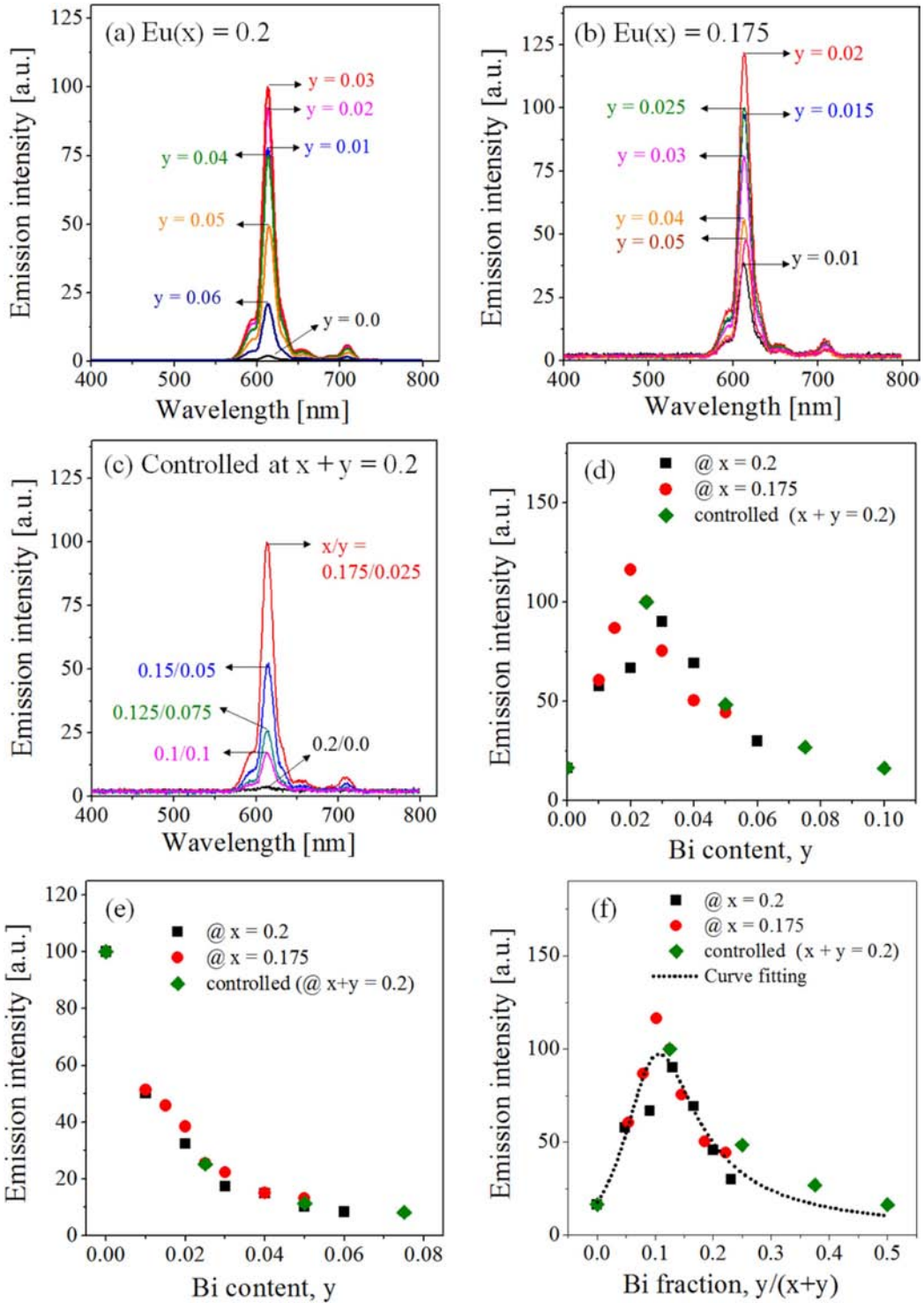

Fig. 4. Luminescence spectra of $Gd_{2-x-y}O_3:Eu_x/Bi_y$ particles with the change of the Bi content (y) at x = 0.2 (a), 0.175 (b), and (c) x + y = 0.2. Changes in the emission intensity with respect to the Bi content ((d) λ_{ex} = 342 nm and (e) λ_{ex} = 254 nm) and the Bi fraction (f).

shows the emission intensities with respect to the Bi^{3+} content (y). The optimum Bi^{3+} content differs slightly depending on the Eu^{3+} content; however, concentration quenching occurs when the Bi^{3+} content (y) is greater than or equal to 0.02. According to the results presented thus far, the optimum Eu^{3+} (x) and Bi^{3+} (y) contents were determined as x = 0.175 and y = 0.02 in order to maximize the red emission intensity under the 342-nm UV excitation. Fig. 4(e) shows the emission intensity of Gd_2O_3:Eu^{3+}/Bi^{3+} under the 254-nm UV excitation. Regardless of the Eu^{3+} content, the emission intensity due to the $O^{2-} \rightarrow Eu^{3+}$ charge transfer is reduced dramatically with the increase of the Bi^{3+} content. Fig. 4(f) shows the emission intensity with respect to the Bi fraction. All the data fall well into one volcano curve, in which the emission is maximized at the Bi^{3+} fraction of 0.1. Therefore, for maximizing the energy-transfer efficiency, the optimum Bi^{3+} percentage is approximately 10.0% of the total doping quantity.

At a fixed Eu^{3+} content less than the critical concentration, the probability of energy transfer from Bi^{3+} to Eu^{3+} is expected to increase as the Bi^{3+} concentration increases. Nevertheless, there is luminescence quenching, indicating that non-radiative energy transfer occurs when the Bi^{3+} content is > 0.02. In Gd_2O_3:Eu^{3+}/Bi^{3+}, non-radiative energy transfer between Eu^{3+} ions or between Bi^{3+} ions is possible. In this study, the Eu^{3+} concentration used for the Bi co-doping experiments was lower than the critical concentration (x = 0.2). Therefore, it can be assumed that the luminescence quenching is not due to non-radiative energy transfer through dipole–dipole interactions between Eu^{3+} ions. To confirm this, the plots of $\ln(I/x)$ vs. $\ln(x_{Eu+Bi})$ and $\ln(I/y_{Bi})$ vs. $\ln(y_{Bi})$ are shown Figs. 5(a) and (b), respectively. As shown in Fig. 5(a), the slopes are - 6.97 and - 9.0 for x_{Eu} = 0.2 and x_{Eu} = 0.175, respectively. The resulting Q values are significantly larger than 2. Thus, it is considered that the distance between Eu ions due to the Bi addition becomes larger and the luminescence quenching is not due to the dipole–dipole interaction between Eu^{3+} ions. On the other hand, in the plot of $\ln(I/y_{Bi})$ vs. $\ln(y_{Bi})$, all data fall in a straight line, whose slope is approximately - 2.28 (Q = 7.08). Therefore, dipole–dipole or dipole–quadrupole interactions between Bi^{3+} ions are involved in the non-radiative energy transfer. Then, the critical distance between Bi^{3+} ions, calculated at the critical concentration (y = 0.02), is approximately 19.6 Å.

3.3. Synthesis of nanosize Gd_2O_3:Eu/Bi and luminescent pearl pigments

To prepare Gd_2O_3:Eu/Bi nanoparticles, EG was added to the precursor solution. The luminescence intensity monitored by varying the mole ratio of EG to Gd in the precursor solution is shown in Fig. 6. The emission intensity decreases slightly with the increase of the EG/Gd ratio. Compared with the sample prepared without EG, the samples pre-

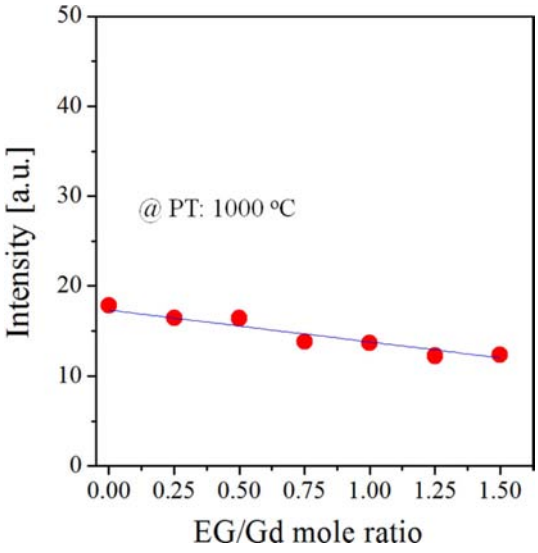

Fig. 6. Emission intensity of Gd_2O_3:Eu/Bi phosphor prepared via spray pyrolysis with respect to the EG/Gd mole ratio.

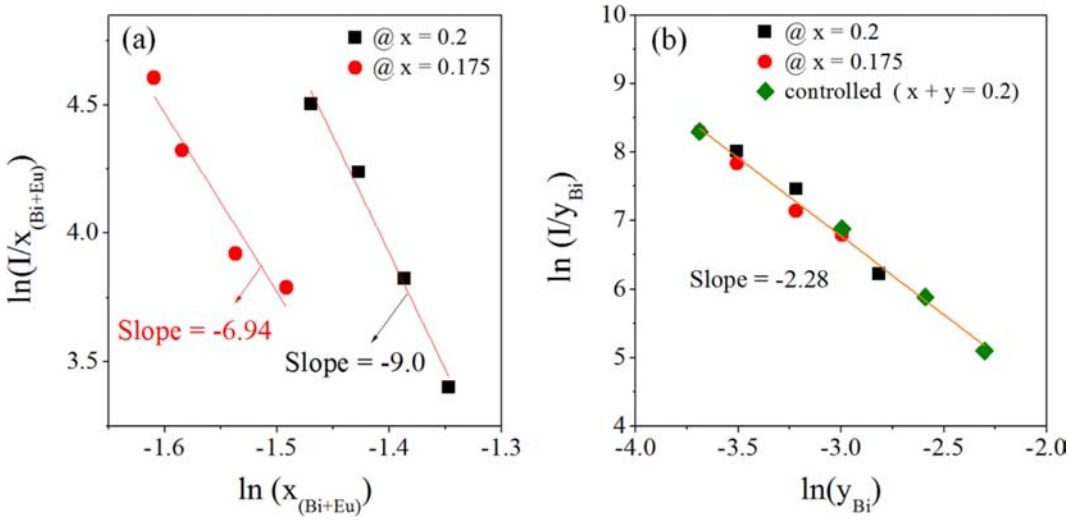

Fig. 5. Plots of (a) $\ln(I/x_{Bi+Eu})$ vs. $\ln(x_{Bi+Eu})$ and (b) $\ln(I/y_{Bi})$ vs. $\ln(y_{Bi})$ for Gd_2O_3:Eu/Bi phosphor.

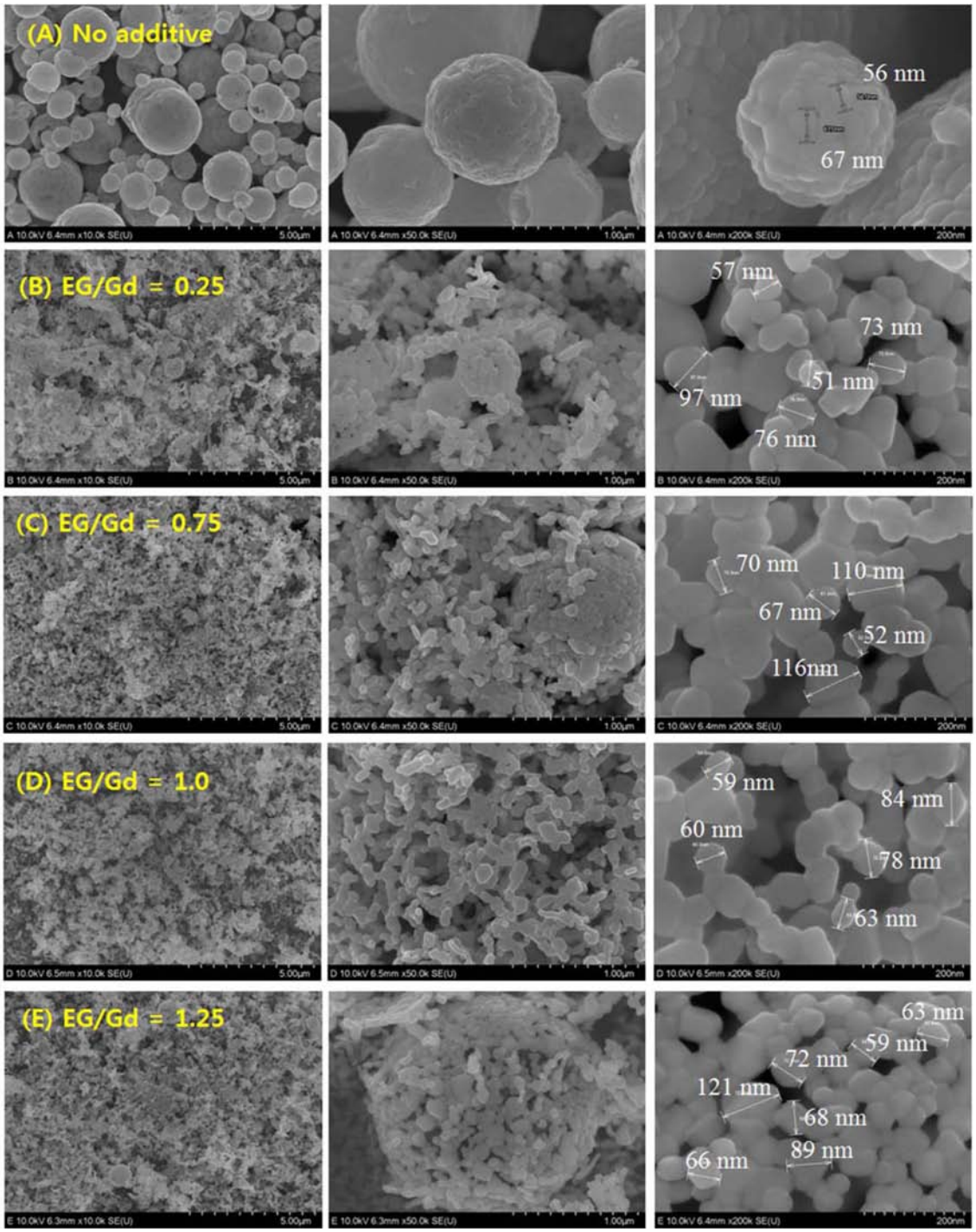

Fig. 7. SEM images of Gd_2O_3:Eu/Bi particles prepared by changing the EG/Gd mole ratio.

pared at EG/Gd = 1.25 have approximately 30% lower intensity. The changes in the particle morphology and size of the Gd_2O_3:Eu/Bi powder prepared by changing the EG/Gd mole ratio were monitored via SEM, and the results are shown in Fig. 7. When no EG was used, the prepared particles had a spherical morphology and a size of 1–2 μm. When EG was used, the microsize particles were turned into nanosize particles. This change in morphology and size occurred because the EG additive used had a significant impact on the formation of particles in the spray pyrolysis process. The influence of organic additives on particle formation mechanism in spray pyrolysis processes is well described in the prior literature.[29,33] When droplets pass through the hot reactor, the water evaporation occurs rapidly and increases the salt concentration. Owing to the rapid drying, the salt concentration at the surface of the droplet first reaches the

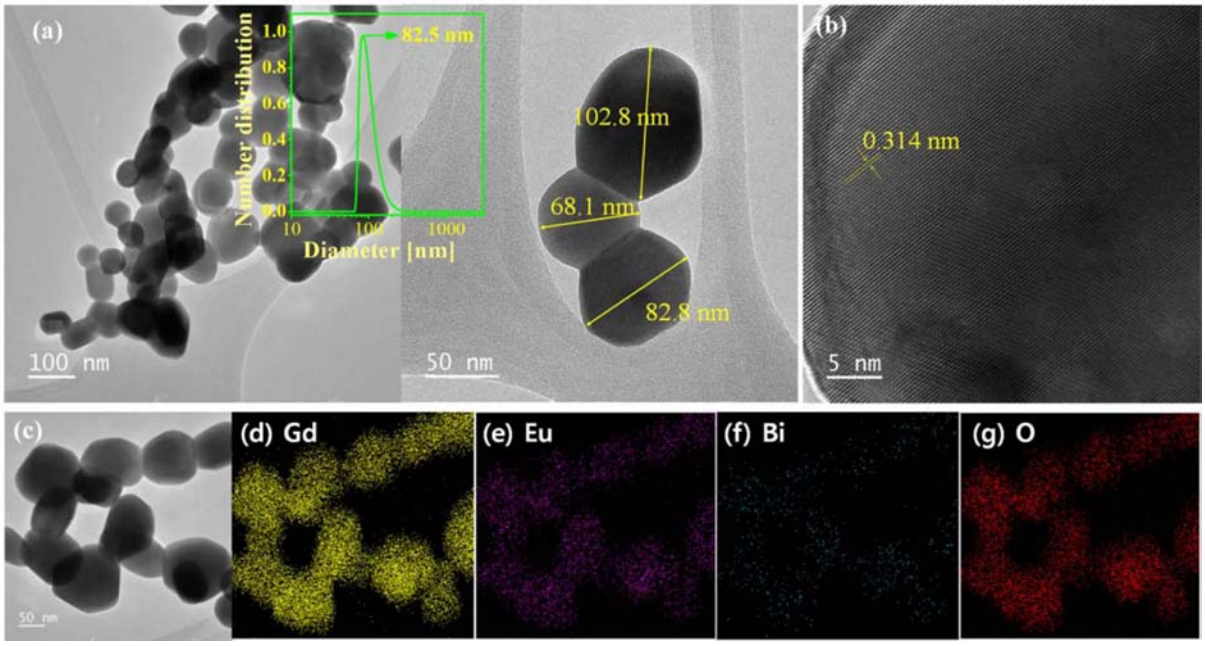

Fig. 8. TEM images (a and b) and element mapping (c–g) of Gd_2O_3:Eu/Bi nanoparticles prepared at EG/Gd = 1.25 (mole ratio).

supercritical point. As a result, surface precipitation occurs, and a thin shell with a precursor solution is formed. The boiling point of EG is higher than that of water. Thus, EG does not evaporate while water is evaporating. As a result, EG remains in the shell layer with the precipitated salts and makes the precipitated layer sticky and supple. Evaporation of additional water or the generation of pyrolysis gas increases the internal pressure, inflating the initially formed shell layer similar to a balloon. After drying and pyrolysis are completed, the produced particles have a hollow structure with a thin layer. Finally, the post-calcination crystallizes the thin layer into less agglomerated nanoparticles. As shown in Fig. 7, no significant change in the primary particle size was observed by increasing the EG/Gd ratio. Fig. 8 shows TEM images of the Gd_2O_3:Eu/Bi nanoparticles synthesized at the EG/Gd mole ratio of 1.25. To measure the particle-size distribution, the produced Gd_2O_3:Eu/Bi nanoparticles were dispersed in water and treated by ultrasonic pulverization. The inset of Fig. 8(a) shows the particle-size distribution. The pulverized powder has a narrow size distribution with a full width at half maximum of approximately 40 nm, indicating that the aggregation between the primary particles is weak and can be easily disintegrated by simple ultrasonic pulverization. The average particle size is approximately 82.5 nm, which agrees well with the TEM result. The high-resolution TEM image shown in Fig. 8(b) indicates that the Gd_2O_3:Eu/Bi particles have high crystallinity and a lattice spacing of 0.314 nm, corresponding to the (222) crystal planes of cubic Gd_2O_3. Figs. 8(d)–(g) show the element mapping images, indicating that the elements Eu and Bi are uniformly distributed in the Gd_2O_3 host.

The prepared Gd_2O_3:Eu/Bi nanoparticles were coated on the surface of plate-shaped pearl substrates (TiO_2-coated alumina). Fig. 9(a) shows SEM photos of the resulting pearl powder prepared by varying the coating weight of Gd_2O_3:Eu/Bi nanoparticles from 5 to 15 wt.%. The SEM results confirmed that the phosphor nanoparticles were well-distributed on the surface of the pearl substrates, as shown in the schematic diagram of Fig. 9(b). The emission properties of pearl pigments coated with Gd_2O_3:Eu/Bi nanoparticles were measured under the 365-nm UV excitation, and the resulting spectra are shown in Fig. 9(c). The prepared pearl powder coated with Gd_2O_3:Eu/Bi nanoparticles has good red emission, and its emission intensity increases linearly with respect to the coating weight of Gd_2O_3:Eu/Bi nanoparticles. Fig. 9(d) shows the "KNU" logo printed on a black plastic panel using pearl pigments coated with the prepared Gd_2O_3:Eu/Bi nanoparticles. No significant difference was observed in the pearlescent logo under natural light. Therefore, the presence of the fluorescent nanoparticles cannot be detected under normal natural light. On the other hand, the pearlescent logo showed red color under the illumination of a portable UV LED lamp (λ_{em} = 365 nm), and its red luminescence became more intense as the coating weight increased. Given this, the pearl logo prepared using pearl pigments coated with Gd_2O_3:Eu/Bi nanoparticles has high red emission that is visible to the naked eye, indicating that the pearl logo has its own anti-counterfeiting function without additional security markers such as quick-response codes.

4. Conclusions

Gd_2O_3:Eu/Bi nanoparticles were synthesized via spray pyrolysis using EG as an organic additive, and the lumines-

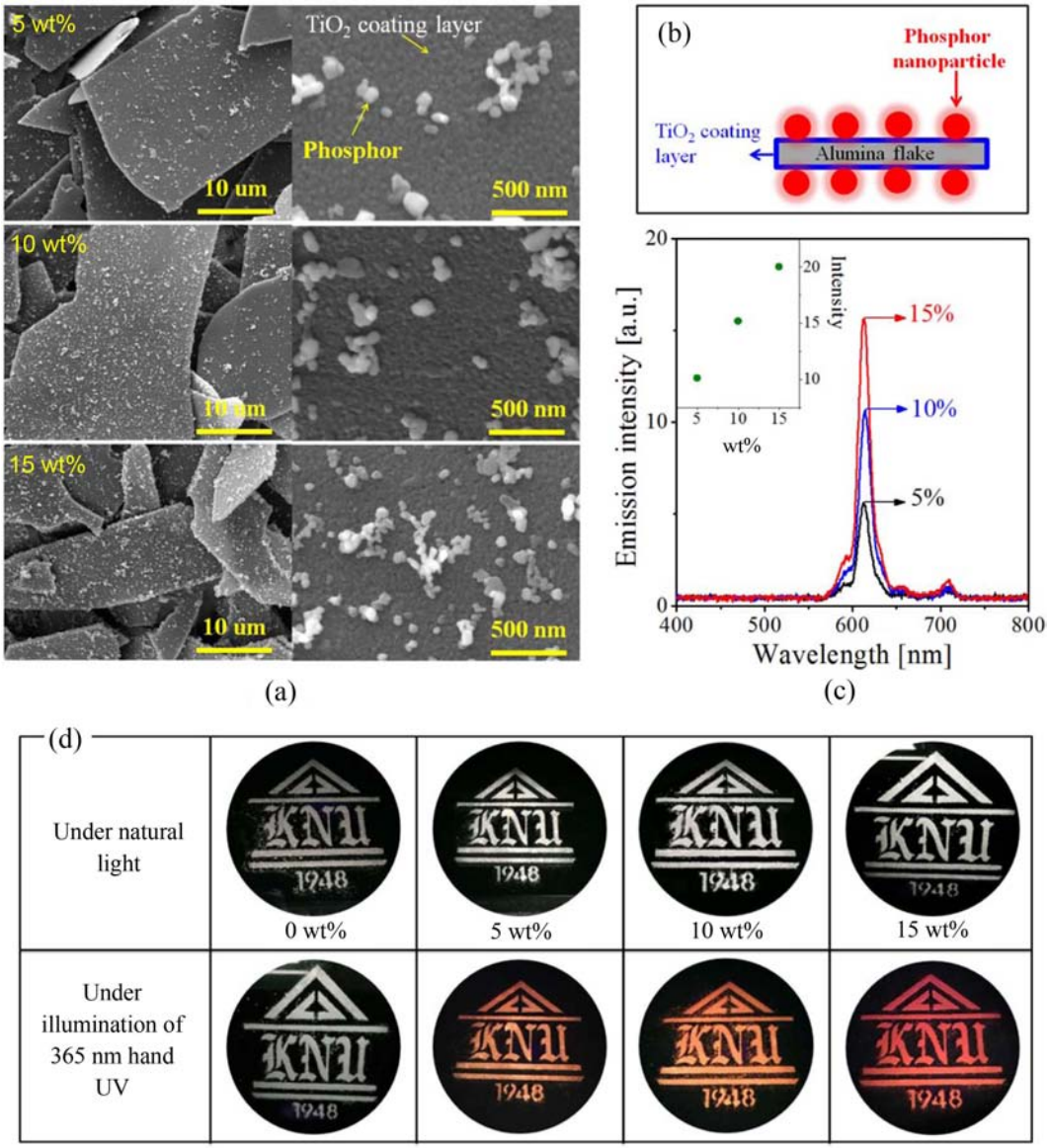

Fig. 9. (a) SEM images, (b) schematic diagram of the phosphor-coated pearl pigment, (c) emission spectra measured at λ_{ex} = 365 nm for pearl substrates coated with Gd_2O_3:Eu/Bi particles, and (d) optical images of the printed "KNU" logo under natural light and illumination from a 365-nm portable LED UV lamp.

cence properties were optimized by changing the Eu and Bi concentrations. Gd_2O_3:Eu/Bi was found to have significantly enhanced red emission compared with Gd_2O_3:Eu owing to the energy transfer from Bi^{3+} to Eu^{3+} under 365-nm UV excitation. For obtaining the highest emission intensity, the optimum Eu^{3+} and Bi^{3+} contents were determined as x = 0.175 and y = 0.02 in $Gd_{2-x-y}O_3$:Eu_x/Bi_y. The use of EG made it possible to produce Gd_2O_3:Eu/Bi nanoparticles with no significant aggregation, and the resulting powders had a size of approximately 82.5 nm and a narrow size distribution. The prepared Gd_2O_3:Eu/Bi nanoparticles were coated on the surface of the pearl pigment, and the resulting powder was found to have sufficiently high red emission to be visible to the naked eye under a 365-nm portable LED lamp. Therefore, it was concluded that the optimized Gd_2O_3:Eu/Bi nanoparticles prepared via spray pyrolysis have excellent luminescence properties and can be applied for the production of luminescent pearl pigments having their own anti-counterfeiting function.

Acknowledgments

This work was supported by the Technology Innovation Program (Advanced Technology Center, ATC) funded by the Ministry of Trade, Industry & Energy, Republic of Korea (Grant no. 10052088).

REFERENCES

1. Y. Cui, R. S. Hegde, I. Y. Phang, H. K. Lee, and X. Y. Ling,

"Encoding Molecular Information in Plasmonic Nanostructures for Anti-Counterfeiting Applications," *Nanoscale*, **6** [1] 282–88 (2014).
2. K. Jiang, L. Zhang, J. Lu, C. Xu, C. Cai, and H. Lin, "Triple-Mode Emission of Carbon Dots: Applications for Advanced Anti-Counterfeiting," *Angew. Chem., Int. Ed.*, **55** [25] 7231–35 (2016).
3. L. Li, "Technology Designed to Combat Fakes in the Global Supply Chain," *Business Horizons*, **56** [2] 167–77 (2013).
4. S. L. Sonawane and S. K. Asha, "Fluorescent Polystyrene Microbeads as Invisible Security Ink and Optical Vapor Sensor for 4-Nitrotoluene," *ACS Appl. Mater. Interfaces*, **8** [16] 10590–99 (2016).
5. M. You, M. Lin, S. Wang, X. Wang, G. Zhang, Y. Hong, Y. Dong, G. Jin, and F. Xu, "Three-Dimensional Quick Response Code Based on Inkjet Printing of Upconversion Fluorescent Nanoparticles for Drug Anti-Counterfeiting," *Nanoscale*, **8** [19] 10096–104 (2016).
6. H. Kang, J. W. Lee, and Y. Nam, "Inkjet-Printed Multi-wavelength Thermoplasmonic Images for Anticounterfeiting Applications," *ACS Appl. Mater. Interfaces*, **10** [7] 6764–71 (2018).
7. T. Sun, B. Xu, B. Chen, X. Chen, M. Li, P. Shi, and F. Wang, "Anti-Counterfeiting Patterns Encrypted with Multi-Mode Luminescent Nanotaggants," *Nanoscale*, **9** [8] 2701–5 (2017).
8. Y. Liu, K. Ai, and L. Lu, "Designing Lanthanide-Doped Nanocrystals with Both Up- and Down-Conversion Luminescence for Anti-Counterfeiting," *Nanoscale*, **3** [11] 4804–10 (2011).
9. P. Kumar, J. Dwivedi, and B. K. Gupta, "Highly Luminescent Dual Mode Rare-Earth Nanorod Assisted Multi-Stage Excitable Security Ink for Anti-Counterfeiting Applications," *J. Mater. Chem. C*, **2** [48] 10468–75 (2014).
10. P. Kumar, S. Singh, and B. K. Gupta, "Future Prospects of Luminescent Nanomaterials Based Security Inks: from Synthesis to Anti-Counterfeiting Applications," *Nanoscale*, **8** [30] 14297–340 (2016).
11. M. Wang, Z. Huang, Z. Guo, and W. Yang, "Luminescent Metal Clusters/Barium Sulfate Composites for White Light-Emitting Devices and Anti-Counterfeiting Labels," *RSC Adv.*, **8** [6] 2866–71 (2018).
12. F. J. Maile, G. Pfaff, and P. Reynders, "Effect Pigments-Past, Present and Future," *Prog. Org. Coat.*, **54** [3] 150–63 (2005).
13. B. Mahltig, J. Zhang, L. Wu, D. Darko, M. Wendt, E. Lempa, M. Rabe, and H. Haase, "Effect Pigments for Textile Coating: a Review of the Broad Range of Advantageous Functionalization," *J. Coat. Technol. Res.*, **14** [1] 35–55 (2017).
14. S. J. Lee, M. S. You, and S. H. Lim, "Formation of Uniform TiO_2 Nanoshell on a-Alumina Nanoplates for Effective Metallic Luster Pigments," *Korean J. Chem. Eng.*, **33** [9] 2732–37 (2016).
15. Y. Wang, M. Liu, Y. Liu, J. Luo, X. Lu, and J. Sun, "A Novel Mica-Titania@Graphene Core-Shell Structured Antistatic Composite Pearlescent Pigment," *Dyes Pigm.*, **136** 197–204 (2017).
16. Q. Gao, X. Wu, and Y. Fan, "Solar Spectral Optical Properties of Rutile TiO_2 Coated Mica-Titania Pigments," *Dyes Pigm.*, **109** 90–5 (2014).
17. M. R. Tohidifar, E. Taheri-Nassaj, and P. Alizadeh, "Precursor Content Assessment and its Influence on the Optical Interference of a Nano-Sized Mica-Hematite Pearlescent Pigment," *Powder Technol.*, **204** [2–3] 194–97 (2010).
18. K. Y. Jung, J. C. Lee, D. S. Kim, B.-K. Choi, and W.-J. Kang, "Co-Doping Effect of Monovalent Alkali Metals on Optical Properties of CeO_2:Eu Nanophosphor Prepared by Spray Pyrolysis and Application for Preparing Pearlescent Pigments with Red Emission," *J. Lumin.*, **192** 1313–21 (2017).
19. A. Saha, S. C. Mohanta, K. Deka, P. Deb, and P. S. Devi, "Surface-Engineered Multifunctional Eu:Gd_2O_3 Nanoplates for Targeted and pH-Responsive Drug Delivery and Imaging Applications," *ACS Appl. Mater. Interfaces*, **9** [4] 4126–41 (2017).
20. W.-N. Wang, W. Widiyastuti, T. Ogi, I. W. Lenggoro, and K. Okuyama, "Correlation between Crystallite/Particle Size and Photoluminescence Properties of Submicronmeter Phosphors," *Chem. Mater.*, **19** [7] 1723–30 (2007).
21. T. Watanabe, Y. Iso, and T. Isobe, "Synthesis of Y_2O_3:Bi^{3+},Eu^{3+} Nanosheets from Layered Yttrium Hydroxide Precursor and Their Photoluminescence Properties," *RSC Adv.*, **7** [23] 14107–13 (2017).
22. X. T. Wei, Y. H. Chen, X. R. Cheng, M. Yin, and W. Xu, "Photoluminescence Characteristics and Energy Transfer between Bi^{3+} and Eu^{3+} in Gd_2O_3:Eu^{3+},Bi^{3+} Nanophosphors," *Appl. Phys. B*, **99** [4] 763–68 (2010).
23. W. Xu, H. Song, D. Yan, H. Zhu, Y. Wang, S. Xu, X. Bai, B. Dong, and Y. Liu, "YVO_4:Eu^{3+},Bi^{3+} UV to Visible Conversion Nano-Films Used for Organic Photovoltaic Solar Cells," *J. Mater. Chem.*, **21** [33] 12331–36 (2011).
24. T. Orihashi, T. Nakamura, and S. Adachi, "Resonant Energy Transfer in (Eu^{3+},Bi^{3+})-Codoped $CaZrO_3$ Red-Emitting Phosphor," *RSC Adv.*, **6** [70] 66130–39 (2016).
25. H. Xiao, P. Li, F. Jia, and L. Zhang, "General Nonaqueous Sol-Gel Synthesis of Nanostructured Sm_2O_3, Gd_2O_3, Dy_2O_3, and Gd_2O_3:Eu^{3+} Phosphor," *J. Phys. Chem. C*, **113** [50] 21034–41 (2009).
26. H. Chen, J. Zhang, X. Wang, S. Gao, M. Zhang, Y. Ma, Q. Dai, D. Li, S. Kan, and G. Zou, "The Effect of the Size of Raw $Gd(OH)_3$ Precipitation on the Crystal Structure and PL Properties of Gd_2O_3:Eu," *J. Colloid Interface Sci.*, **297** [1] 130–33 (2006).
27. X. Ye, W. Gao, L. Xia, H. Nie, and W. Zhuang, "A Modified Solution Combustion Method to Superfine Gd_2O_3:Eu^{3+} Phosphor: Preparation, Phase Transition and Optical Properties," *J. Rare Earths*, **28** [3] 345–50 (2010).
28. B. H. Min and K. Y. Jung, "Synthesis of Luminescence Characteristics of Fine-Sized $Ba_2Si_6O_{12}N_2$:Eu Green Phosphor through Spray Pyrolysis Using TEOS/Si_3N_4 Mixed Precursors," *RSC Adv.,* **7** [71] 44759–65 (2017).
29. J. S. Cho, K. Y. Jung, and Y. C. Kang, "Yolk-Shell Structured Gd_2O_3:Eu^{3+} Phosphor Prepared by Spray Pyrolysis: the Effect of Preparation Conditions on Microstructure and Luminescence Properties," *Phys. Chem. Chem. Phys.*, **17** [2] 1325–31 (2015).

30. M. Borlaf, R. Kubrin, V. Aseev, A. Y. Petrov, N. Nikonorov, and T. Graule, "Deep Submicrometer YAG:Ce Phosphor Particles with High Quantum Yield Prepared by Flame Spray Synthesis," *J. Am. Ceram. Soc.*, **100** [8] 3784–93 (2017).
31. K. Y. Jung, C. H. Lee, and Y. C. Kang, "Effect of Surface Area and Crystallite Size on Luminescent Intensity of Y_2O_3:Eu Phosphor Prepared by Spray Pyrolysis," *Mater. Lett.*, **59** [19–20] 2451–56 (2005).
32. C. H. Lee, K. Y. Jung, J. G. Choi, and Y. C. Kang, "Nano-Sized Y_2O_3:Eu Phosphor Particles Prepared by Spray Pyrolysis," *Mater. Sci. Eng., B*, **116** [1] 59–63 (2005).
33. B. H. Min, J. C. Lee, K. Y. Jung, D. S. Kim, B.-K. Choi, and W.-J. Kang, "An Aerosol Synthesis of CeO_2:Eu^{3+}/Na^+ Red Nanophosphor with Enhanced Photoluminescence," *RSC Adv.*, **6** [84] 81203–10 (2016).
34. R. G. A. Kumar, S. Hata, K.-I. Ikeda, and K. G. Gopchandran, "Luminescence Dynamics and Concentration Quenching in $Gd_{2-x}Eu_xO_3$ Nanophosphor," *Ceram. Int.*, **41** [4] 6037–50 (2015).
35. O. Meza, E. G. Villabona-Leal, L. A. Diaz-Torres, H. Desirena, J. L. Rodríguez-López, and E. Pérez, "Luminescence Concentration Quenching Mechanism in Gd_2O_3:Eu^{3+}," *J. Phys. Chem. A*, **118** [8] 1390–96 (2014).
36. M. Buijs, A. Meyerink, and G. Blasse, "Energy Transfer between Eu^{3+} Ions in a Lattice with Two Different Crystallographic Sites: Y_2O_3:Eu^{3+}, Gd_2O_3:Eu^{3+} and Eu_2O_3," *J. Lumin.*, **37** 9–20 (1987).